Solar wind control of Earth's H^+ and O^+ outflow rates in the 15-eV to 33-keV energy range

O.W. Lennartsson and H.L. Collin

Advanced Technology Center, Lockheed Martin Space Systems Company, Palo Alto, California, USA

W.K. Peterson

Laboratory for Atmospheric and Space Physics, University of Colorado, Boulder, Colorado, USA

Earth's high-latitude outflow of H^+ and O^+ ions has been examined with the TIMAS instrument on the Polar satellite in the 15-eV to 33-keV energy range over an almost three-year period near solar minimum (1996-98). This outflow is compared with solar wind plasma and magnetic field (IMF) data from the WIND spacecraft, the latter having been time shifted to the subsolar magnetopause and averaged for 15 minutes prior to each sampling of Earth's magnetic field-aligned ion flow densities. When the flow data are arranged according to the polarity of the IMF B_z (in GSM coordinates) and limited to times with $B_z > 3$ nT or $B_z < -3$ nT, the total rate of ion outflow is seen to be significantly enhanced with negative B_z, typically by factors of 2.5-3 for the O^+ and 1.5-2 for the H^+, more than previously reported from similar but less extensive comparisons. With either IMF B_z polarity, the rate of ion outflow is well correlated with the solar wind energy flow density, especially well with the density of kinetic energy flow. The rate of ion outflow within the instrument's energy range is a strong function of the Polar satellite altitude, increasing almost threefold from perigee ($R \sim 2$ R_E) toward apogee ($R \sim 4$ to 9 R_E) for O^+ ions,

i.e. up to 10^{26} ions s^{-1} or more per hemisphere. The apogee enhancement may be still larger for the H^+, but it is obscured by mantle flow of cusp-origin solar H^+. Ion mean energy also increases with altitude, leading to about a 20-fold increase in the O^+ energy flow rate from Polar perigee to apogee altitude, reaching values of 20 GW or more per hemisphere. While the perigee outflow of H^+ has little or no seasonal modulation, in terms of ions s^{-1}, the O^+ outflow rates at both altitudes do increase during local summer, and so does the rate of cusp-origin H^+ flow near apogee. The latter rate in fact has very similar seasonal modulation as the O^+ rates, suggesting that it has a significant influence on the O^+ outflow.

1. Introduction

With the flight of ion composition instruments on the Polar satellite, beginning more than eight years ago (Polar launched on 24 February, 1996), adding to several earlier missions of varied orbits, we now have essentially contiguous altitude records of the outflow of energized ionospheric ions, such as the O^+, from $R \approx 2$ R_E (geocentric) to $R \approx 23$ R_E, at least in the energy range from a few tens of eV/e (including the typically positive s/c potential) to a few tens of keV/e. Magnetotail ion composition measurements in that energy range were first made more than 20 years ago on the ISEE-1 satellite, within 23 R_E [*Lennartsson and Shelley*, 1986; and references therein], and are presently being made with the Cluster satellites within 19 R_E [e.g. *Rème et al*., 2001]. Near-Earth ion composition measurements (~2 R_E) were begun even earlier with the polar orbiting S3-3 satellite and were indeed the first to both detect the energetic ion outflow and provide substantial statistical material [e.g. *Ghielmetti et al*., 1978; *Collin et* al., 1981]. Similar measurements were subsequently extended as far as R ~6 R_E with the PROGNOZ-7 satellite [*Lundin et al.*, 1983] and R ~4.5 R_E with the DE-1 satellite [e.g. *Yau et al*.,

1984; *Yau et al*., 1985a and b], the latter being especially pivotal in that they were made continually over almost 10 years, that is almost a complete solar cycle. The initial orbit of the Polar satellite, with its perigee and apogee at $R \approx 2$ R_E above the southern and $R \approx 9$ R_E above the northern polar caps, respectively, enables us to use 15-eV/e to 33-keV/e ion composition data from the Toroidal Imaging Mass-Angle Spectrograph (TIMAS) to fill most of the altitude gap between the DE-1 and ISEE-1 statistical records.

Beside the extended altitude coverage, the Polar measurements are superior to those made on DE 1 in several important respects, as evident when comparing the DE 1 EICS instrument [*Shelley et al*.; 1981] and the TIMAS instrument [*Shelley et al*.; 1995; condensed description in Appendix]. In particular, the much faster TIMAS measurement cycle allows us to retain full energy resolution in the statistical records, as opposed to the three broad energy bands employed with the EICS statistical data base, namely 0.01 to 1, 1 to 4 and 4 to 17 keV/e [e.g. *Yau et al*.; 1984]. The DE-1 statistics, while very large in terms of net ion number flows, provide rather limited information about average ion energies and energy flow rates. The principal conclusion by *Yau et al*. [1985b] on those two subjects is that the outflow of H^+ and O^+ ions was dominated by < 1-keV ions.

According to the several years of ISEE-1 measurements, the virtually omnipresent O^+ ions, arguably the "quintessential" ionosphere-origin ions, have a broad energy distribution in the tail plasma sheet beyond 10 R_E, typically averaging about 3 to 4 keV [*Lennartsson and Shelley*; 1986]. This may be contrasted with the (indirect) DE-1 results just quoted and with the finding in this present study that the mean O^+ energy at $R \sim 2$ R_E, near the Polar perigee, is only about 0.1 to 0.4 keV. Interestingly, the mean energy of up-flowing O^+ ions has already increased to between one and two keV by the time they have reached well above $R \sim 4$ R_E, as it turns out, while at the

same time the hemispheric flow rate (ions per second) at energies above the nominal 15 eV minimum (plus s/c potential) has also increased substantially, implying that the acceleration process is operating over a large range in altitude and is not limited to the plasma sheet proper. Unlike the DE-1 and ISEE-1 statistical results, however, these new Polar results are limited to near-minimum solar-cycle conditions, having been obtained during the first three years of TIMAS operations, 1996-98.

The present study takes a different statistical approach to the Sun-Earth connection than did all of the DE-1 studies and most of the ISEE-1 studies. Thus, rather than relying solely on ground-based geomagnetic and solar indices for subdividing the many measurements of ion flow rates and composition, it takes the more direct approach of incorporating high time-resolution observations made by solar wind monitors, specifically those made by the WIND spacecraft. Some of the later ISEE-1 studies did make comparisons between magnetospheric observations and conditions in the solar wind, but the solar wind data were then readily available only at one-hour resolution. One of those, by *Lennartsson* [1995], has in fact provided some of the incentive for doing this study in the first place, since the ISEE-1 results from the near-equatorial plasma sheet seem to show weaker correlation between the O^+ concentration and the north-south polarity of the interplanetary magnetic field (IMF) than might be expected from the rather strong correlation between the O^+ and the geomagnetic indices, such as the Kp and the AE.

Of special interest when trying to understand the energizing of ion outflows is to know the concurrent solar wind power input in true physical units, kinetic as well as electromagnetic. However, even without that understanding, merely having some statistical measures of the relationship may simplify the incorporation of ionospheric ion outflows in global numerical simulations of the Sun-Earth connection.

2. Field-Aligned Ion Flows

2.1. Sampling the Flow Density

By magnetic field-aligned flow density $F_{||}$ (e.g. $m^{-2}s^{-1}$) we envision the following integral,

$$F_{||} = 2\pi \iint J(E,\_) \cos\_ \sin\_ \, d\_ \, dE$$

where J is the differential number flux (usually in $cm^{-2}s^{-1}ster^{-1}(keV/e)^{-1}$) of ions with the same M/Q, and E and _ are the energy per charge (E/Q) and pitch angle, respectively, of some arbitrary ion in that category, assuming there is no other angular dependence. The integral in energy is to be across the instrumental range, and that in pitch angle to be from 0° to 180°, except that we wish to exclude flux within the nominal atmospheric loss cone on the earthward side, as explained below. We approximate this double integral with the following double sum,

$$F_{||} \approx 2\pi \, \__i \, \_E[i] \, \{\__n \, J[i,n] \cos\_[n] \sin\_[n] \, \pi \, 12^{-1}\} \qquad (1)$$

where i counts the 28 energy channels, n counts 12 pitch angles, 7.5°, 22.5°, 37.5°, .., 172.5°, and $J[i,n]$ is the average flux (corrected for detector background) in energy channel i and within the pitch-angle interval $\alpha[n]-7.5°$ to $\alpha[n]+7.5°$ during a 12-second (two spins) or 24-second interval, depending on altitude. We use 12-second sampling intervals when the geocentric distance $R < 4$ R_E and 24-second intervals when $R \geq 4$ R_E. The summation steps $\_E[i]$ overlap with the respective energy channel width, but are adjusted in size to ensure a contiguous set of

energy intervals. In analogy with 1, we approximate the field-aligned energy flow density $EF_{||}$ with

$$EF_{||} \approx 2\pi \__i \; E[i] \; \_E[i] \; \{\__n \, J[i,n] \cos\_[n] \sin\_[n] \; \pi \; 12^{-1}\} \qquad (2)$$

where $E[i]$ is the center energy of channel i.

The following statistical presentation only invokes this second sum implicitly to define a "flow-weighted" mean ion energy $\langle E \rangle$ by the ratio

$$\langle E \rangle = EF_{||} \; / \; F_{||} \qquad (3)$$

This quantity varies less than the energy flow density does and so allows for condensed graphs. However, rather than calculating 3 for each flow sampling and averaging that ratio across each polar region, we derive average hemispheric flow rates for both energy and ion numbers and display the ratio between those two rates as the "mean energy". That way the reader may infer the total hemispheric rates of energy outflow by multiplying the ion outflow rates, as displayed, with the respective energy.

2.2. Discarding Precipitating Ions

To obtain as true a measure as possible of the outward flow of ions from Earth it is necessary to exclude precipitating ions from the summations in equations 1 and 2, that is to artificially reduce the flux J within some local "loss cone" in the earthward direction. This accounts for such effects as charge exchange with exospheric hydrogen. We recognize that this "cone" in fact has

fuzzy edges that depend on several variables, including ion energy and species, parallel electric potential differences $\_V$, as well as atmospheric composition and scale height. However, we adopt the simplistic model of $\_V = 0$, one single and constant loss altitude h_L and set the flux J equal to zero within the associated cone, that is within a pitch-angle range defined, respectively for southern and northern latitudes, by

$$180° - \arcsin (B/B[h_L])^{1/2} < \_ \leq 180° \qquad (4a)$$

$$\_ < \arcsin (B/B[h_L])^{1/2} \qquad (4b)$$

where $B[h_L]$ is the geomagnetic field strength at the loss altitude and B is the field measured at the satellite [*Russell et al.*, 1995]. This is the same approach as that taken by *Yau et al.* [1985b], who find the net ion outflow rates to be rather insensitive (within a few percent) to the choice of h_L within a few hundred km (and $\_V \sim$ few hundred V). We are using $h_L = 400$ km here, which makes a loss-cone half-angle of less than 25° around the southern perigee of Polar, and about 7° or less in the northern hemisphere. The angle derived with each sampling is used for removing part or all of certain terms in the sums 1 and 2, in proportion to the corresponding solid angle.

2.3. Normalizing Flow Densities

Deriving a global outward flow rate from multiple samplings at varying distance from Earth is facilitated by first normalizing flow density to some more or less arbitrary common altitude, h_N, assuming that (*i*) field-aligned flow density is proportional to the local magnetic field B and (*ii*) the field $B[h_N]$ at that one altitude can be inferred in a meaningful fashion, for example by tracing a field line through the Polar position toward Earth. For simplicity, we are assuming that

cross-field ion drift, particularly **E×B** drift, can be neglected and that ions moving away from the ionosphere indeed do follow magnetic field lines. This issue will be addressed later (Section 6.1) in the context of estimating error margins. As far as h_N is concerned, we use the value 300 km here.

2.4. Assigning Magnetic Footprints

Although we invoke the magnetic conjunction between the Polar satellite and a presumed near-Earth ion source for both the normalizing of flow densities and the calculation of loss cones, we do not believe the accuracy of our assumptions and flow calculations, nor that of standard field line tracing procedures for that matter, warrant a tracing for every 12- or 24-second sampling, being that our samplings number in the millions. Instead, we utilize an existing and approximate set of "footprint" Key Parameters produced by the Polar Magnetic Field Experiment (MFE) Team [*Russell et al.*, 1995] with the IGRF-95 internal and TSY-95 external field models [cf. *Tsyganenko*, 1995]. These are in geographic (GEO) coordinates, refer to Earth's ground level, have 0.92-minute resolution, and were all derived under the assumption of zero Dst and a constant 2 nPa solar wind dynamic pressure (see http://www-ssc.igpp.ucla.edu/polar/ for further details).

From these coordinates we infer the magnetic field strengths at h_N and h_L with the help of Tsyganenko's GEOPACK-2003 codes obtained from the National Space Science Data Center (NSSDC) Web site (http://nssdc.gsfc.nasa.gov/space/model/magnetos/data-based/). For northern hemisphere samplings we use the same set of codes to transform the foot-print position to magnetic local time (MLT) and invariant latitude (INV LAT), which are the coordinates we use to bin the flow data. For southern, near-perigee samplings, however, we use the standard Polar

ephemeris eccentric-dipole EDMLT and INV LAT coordinates for binning, since those in fact order the TIMAS data better when Polar is that close to Earth (and the ambient field is indeed dipole-like).

2.5. False Outward Flow Samplings

There are at least three ways the sums in 1 and 2 may indicate outward flow for the wrong reasons:

a. Non-uniform Flux

As illustrated by *Lennartsson et al.* [2001], the ion flux observed in the Polar frame of reference, by the TIMAS instrument, may vary substantially on a time scale of 12 seconds, often by orders of magnitude, suggesting large variations on even shorter time scales. Since the flow density sums contain terms from different spin phases, the apparent flow may reflect spatial gradients rather than local anisotropy.

b. Magnetospheric Ion Bursts

That same TIMAS study also revealed that earthward, few-minute duration bursts of energetic (> few keV/e) ions, especially H^+ ions, are quite common in the auroral regions. These appear with earthward flow direction initially (and maximum energy), but they always occupy pitch angles beyond the local loss cone and may become dominated by mirroring ions within a minute or more. A flow sampling of 24-second duration, or shorter, is likely to mark the mirroring stage as net outward flow. This probably has the greatest impact on the H^+ samplings, especially the samplings of H^+ energy flow density, since these bursts are 10 to 30 times more energetic than the typical ionosphere-origin H^+ ions. These bursts are in fact regularly associated with enhanced

outward flows of ionospere-origin H^+, O^+ and He^+ ions [*Lennartsson*, 2003], but the net field-aligned number flow densities are normally dominated by the latter ions (see also *Yau et al*. [1985b]). A related but different issue with ion flows in the high-altitude (northern) cusp is dealt with below.

c. Tainted Background Subtraction

This is of main concern when the signal-to-background ratio is low, like in the radiation belts, and much of the error falls within the realm of counting statistics. However, as explained in the Appendix (A.2), there are other possible but inadequately understood reasons for subtracting the wrong background at times, and data with the most extreme background have therefore been excluded (a few per cent of all data).

These potential sources of errors are all difficult or impossible to characterize by error bars a priori. On the other hand, the likely errors are apparently random in direction with respect to up or down, so one may appraise the effects by comparing sums of unidirectional samplings with sums of randomly directed ones. By the same token, the errors will tend to cancel out in large sums of bi-directional samplings.

3. Solar Wind Power Input

Considering the solar wind-magnetosphere-ionosphere interactions with conservation laws in mind, one may argue that the most fundamental input for driving the ion outflow must be the solar wind flow density of energy, be it kinetic or electromagnetic, since the material source is the ionosphere. Whether this driving can be readily manifested in statistical terms may depend on subtle details, such as adequate averaging and selection of proper time shifts between

measures of cause and effect, and on having the solar wind monitor sufficiently close to the Sun-Earth line, of course, preferably upstream (c.f. *Collier et al*. [1998]).

Since the peak upwelling, 10-eV type O^+ flux, on the dayside, is known to be better correlated with the preceding hourly standard deviation of a solar wind parameter, such as dynamic pressure (time shifted to Earth), than with the hourly mean parameter itself [*Moore et al.*, 1999; *Pollock et al.*, 1990], it is probably preferable to compare our 12- and 24-second samplings with solar wind averages that are shorter than an hour. Using the approximately two-minute WIND Key Parameters [*Ogilvie et al.*, 1995; *Lepping et al.*, 1995] individually, on the other hand, is most likely less than optimal, because the observed ion outflows at Polar may represent longer travel times than that from the source, ranging from a few seconds to several minutes at perigee, with low-energy O^+ ions being the slowest. As a compromise, we use 15-minute averaging here. We count time backward from each TIMAS sampling and average corresponding solar wind parameters that have been time shifted to the subsolar magnetopause (see Appendix A3).

We use the same last-15-minutes WIND averaging with Polar data from both the southern perigee altitude and the northern near-apogee altitudes for two reasons: (*i*) This allows us to compare outflows from both hemispheres under essentially identical solar wind conditions, and (*ii*) the O^+ ions, as it turns out, have about five times higher mean energy near apogee, thus traveling further in a given time. Specifically, O^+ ions with the typical northern hemisphere energy of 1 keV may travel as far as 15 R_E in 15 minutes, well beyond the 9 R_E Polar apogee. Furthermore, most of the measured ion energy was actually acquired a few R_E above the ionosphere, thus probably reflecting solar wind power input since less than 15 minutes ago in most cases.

We adopt the following approximate scalar measures K and S of, respectively, the solar wind kinetic energy flow density **K** and Poynting flux **S**, as defined via geocentric solar-magnetospheric (GSM) coordinates:

$$K = [\mathbf{K}]_x \approx 2^{-1}\, p\, v \qquad (5)$$

$$S = [\mathbf{S}]_x = \__0^{-1}\, [\mathbf{E}\times\mathbf{B}]_x \approx \__0^{-1}\ v\,(B_y^2 + B_z^2) \qquad (6)$$

where p is the dynamic pressure, v the bulk flow speed, $\__0$ the magnetic permeability of vacuum, and B_y and B_z are components of the interplanetary magnetic field (IMF). The first formula, 5, ignores the small (~2%) contribution from solar wind proton and electron thermal motion, and both ignore bulk flow aberration, including the ~30 km s^{-1} Earth orbital speed.

4. MLT-INVL Views of Normalized Flow Density

Figure 1 shows examples of normalized ($\propto B$) upward flow densities, including those of He^+ ions, averaged over the minimum six-month period required for complete coverage in Magnetic Local Time (MLT; noon is up). Each such period is approximately centered on the solstices, in this case representing adjacent "summer seasons" in both the northern, April-September, and southern, October-March, hemispheres. The averaging, within bins of 1-hr MLT by 1° Invariant Latitude, has been carried out without regard to either geomagnetic activity or solar wind conditions. Unlike most of the subsequent figures (4 - 8), it has equated each earthward flow density sample with zero flow by incrementing the counter without adding to the flow density

sum. The reason for the latter is to simplify certain North-South comparisons of proton flows, by excluding earthward (negative) proton flow in the cusp proper (Section 6.2 below).

The binning in the bottom (southern) plots is done with the eccentric dipole EDMLT and INVLAT supplied with the Polar satellite ephemeris. These organize the TIMAS data better here, providing a somewhat sharper separation between auroral zone and polar cap, than do the approximate magnetic footprints described above (2.4). The footprints, however, have been used with the IGRF-95 internal field model to infer the near-Earth magnetic field strength (for computational simplicity). In the top (northern) plots, on the other hand, the binning is done from the footprints, via (centered) dipole coordinate rotations. Despite some blurring about the North Magnetic Pole, the footprints do place the center of the cusp (maximum H^+ density) at a more realistic latitude (< 80°), for instance, than do the ephemeris dipolar coordinates (> 80°; not shown).

With Figure 1 we wish to illustrate the following common topographical aspects of the data: (*i*) In the bottom plots, near perigee altitude, the ion outflow, on average, peaks both in the nightside auroral zone, at least for O^+ and H^+ ions, and about the cusp (or cleft). (*ii*) The cusp enhancement is still more pronounced in the top plots, at much higher altitudes, in particular for H^+ ions, which are apparently dominated by plasma mantle ions here (scaled in flow density to h_N). (*iii*) Outside the cusp region in the top (northern) H^+ plot, around the auroral zone, the mainly green shade corresponds to the top end (red shade), and beyond, of the color bar in the bottom H^+ plot, indicating substantially elevated outflow rate of ionospheric H^+ at these high altitudes (within the instrument energy range).

5. Hemispheric Rates of O^+ and H^+ Outflow

Henceforth our statistical results refer to spatially integrated, or "hemispheric", rates of ion outflow, that is average numbers of ions leaving Earth's vicinity each second above some specified invariant latitude. These rates, in effect, are obtained by adding all flow densities from grids like those in Figure 1, while multiplying each element with its surface area at the normalizing altitude h_N. The statistics are limited to the two dominant species, O^+ and H^+.

5.1. Seasonal Variation

Figure 2 summarizes the average O^+ and H^+ flow rates during each of five six-months seasons (1996-98) in each hemisphere, while grouping the samplings according to the polarity of the average IMF B_z (in GSM) during the preceding 15 minutes (Section 3). While the two hemispheres differ the most with respect to the H^+ (right panel), the O^+ flow rates (left panel) are nevertheless substantially larger in the northern hemisphere, near apogee, than they are in the southern hemisphere, by factors of 2.5 to 4. As with Figure 1, all flow density samplings with earthward direction have been included as "zero outward flow", rather than negative flow.

It should be noted that the much enhanced outward flow rates of H^+ ions in the northern hemisphere, as compared with the southern counterparts, are largely due to ions flowing away from the northern cusp, as illustrated in Figure 1, apparently coming from the solar wind (He^{++} ~ 3% or greater, not shown). The seasonal variation of these rates and of the O^+ rates will be interpreted later (Section 6.2). For seasonal variation of the southern hemisphere outflow of He^+ ions, see *Peterson et al.* [2001].

5.2. Response to Solar Wind Power Input

To derive statistical relationships between a hemispheric outflow rate and some external events, using local flow density samplings, requires that each sampling be weighted, one way or another, by the inverse of the probability of making it, given its latitude and longitude along with the current orbital parameters of the observing platform. This makes a scatter diagram somewhat impractical. Instead, we choose to average and sum multiple times over the same latitude-longitude grid, while accepting flow density samplings contingent on certain solar wind parameters lying within a series of successive specified bounds. To ensure that every grid element is always sampled, we use a much coarser grid than in Figure 1, namely 5° Invariant Latitude, above 55°, by 6 hours of Magnetic Local Time (0-6, etc.), that is a 28-bin grid.

As one of our selection criteria, we continue to use the polarity of the preceding 15-minute average IMF B_z. However, in view of the somewhat modest B_z dependence in Figure 2, mostly less than a factor of two, we impose the stronger requirement that $B_z > 3$ nT and $B_z < -3$ nT in successive runs. This does impact the minimum possible values of both the solar wind Poynting flux S and the kinetic energy flow density K, although not seriously. It also excludes a very large portion of the data, almost 75%, but our grid is replenished by blending all five seasons in each hemisphere (plus several weeks before and after). This means that the southern averages hereafter contain three winters and two summers, and vice versa for the northern averages, a fact that is worth keeping in mind (Figure 2).

Selection by the two solar wind energy flow densities K and S, one at a time (and each averaged over the preceding 15 minutes), must allow for the entire dynamic range of each (limited on the low end by the requirements on B_z). How finely this range can be subdivided is a practical issue, subject to the requirement that our 28 latitude-longitude bins be all filled. Being that a logarithmic division may seem the most “physical”, with at least a factor of three

increments, we have found that no more than three bins are practical. Assuming for the moment the physical unit of _Wm^{-2} for both K and S, our choice is the following set:

$$K < 300, \quad 300 \le K < 1000, \quad 1000 \le K \qquad (7)$$

$$S < 10, \qquad 10 \le S < 30, \qquad 30 \le S \qquad (8)$$

We could allow more than three bins for these parameters by further reducing the number of latitude-longitude bins, but that would make the surface-area weighting of each TIMAS flow density sampling less precise, and the loss of precision would be most severe at the far ends of the K and S ranges. As it is, 7 and 8 ensure that the endpoints are based on adequate sampling.

5.2.1. Southern hemisphere (low altitude). Figure 3 is the first application of this procedure, one that also addresses the issues raised in Section 2.5 above regarding false flow samplings. The left panel, like Figure 2, treats every apparent earthward O^+ flow sampling as one with zero flow density, while the right panel is the result of including all samplings at face value. The main difference between the two panels is with the lowest rates at positive B_z. The sizable difference between different latitude ranges in the left panel (dashed lines) has almost vanished in the right panel, as though there is little O^+ outflow below 65° latitude during times of positive B_z. On the other hand, the TIMAS background count rate normally peaks below 65° latitude, well within the radiation belts (not shown). Therefore, we have good reasons to believe that two of the dashed lines in the left panel reflect false but positive-only contributions from incorrectly subtracted background. By contrast, the right panel allows for these to be cancelled by randomly negative false contributions. The reason this effect is hardly noticeable with negative B_z is almost

certainly an elevated signal-to-background ratio. In any case, all averages in the following figures do include both positive and negative flow density samplings, real or not. It should also be pointed out that the data symbols are overlaid in the order of increasing latitude, sometimes entirely obscuring the circular symbols.

Figure 4 shows a comparison of the same O^+ flow rates ordered by either *K* (upper left panel) or *S* (upper right; different scale for *S*). The bottom panels show the corresponding "mean energies", as defined in Section 2.1 above, although in a condensed fashion. There is some tendency for these "flow-weighted" energies to be larger below 65° latitude than above (cf. *Yau et al.* [1985b]), but differences are not consistent. In order to minimize clutter, the bottom panels here and in subsequent figures treat the three sets of mean energies obtained with flow rates above 55°, 60° and 65° latitude, respectively, as independent measurements of one energy and show the corresponding average by a circular symbol and the standard deviation by an error bar (when larger than the symbol). Note the rather low mean energy of O^+ ions at these near-perigee altitudes.

Figure 5 shows flow rates and energies of H^+ ions, but is otherwise analogous to Figure 4. These southern H^+ rates are on the whole somewhat lower than those of the O^+ ions, and they depend less on the solar wind conditions. The mean energy of the H^+ ions is larger, however. It is conceivable that these "flow-weighted" energies are to some extent contaminated by the "false" energy flow densities associated with energetic magnetospheric H^+ bursts, as surmised in Section 2.5 above (point *b*), but that effect has been minimized by including flow samplings of both signs.

To place Figures 4 and 5 in a broader context, Table 1 lists several environmental parameters that have been averaged along with each of the O^+ flow rates at latitudes greater than 55°,

including the associated IMF B_z and solar wind (SW) parameters *K* and *S* (rounded). That is, the upper left panel of Figure 4 has three open circles connected by solid lines which correspond to the three columns in the top left group of numbers in Table 1 (negative B_z), ordered by increasing *K*, while the three open circles connected by dashed lines correspond similarly to the bottom left group of numbers in Table 1 (positive B_z). Analogously, the open circles in the upper right panel of Figure 4 correspond to the right groups of numbers in Table 1, ordered by *S*. Although these numbers refer specifically to Figure 4, a corresponding table with Figure 5 would look virtually identical. The top two numbers in each of the 12 columns show the number of O^+ flow density samplings and the average geocentric radial distance at which they were made. These are all 12-second (two-spin) samplings. The IMF B_z and all the solar wind (SW) parameters are "smoothed averages" based on the preceding 15-minute running averages described above. From the bottom two numbers in each column it may be noted that the solar wind energy flow densities *K* and *S* are moderately correlated with each other, at least while advancing from midpoint to maximum.

5.2.2. Northern hemisphere (high altitude). The situation is more complex at the northern hemisphere high altitudes, especially with the H^+ ions. As far as O^+ flow rates are concerned, Figure 6 shows a rather similar relative increase with solar wind energy flow densities as Figure 4, but the absolute O^+ rates (different scale) are much higher (within the given energy range), mostly by factors of four to six. At the same time, the mean O^+ energies have increased a great deal as well, by factors of five or more. This means that O^+ energy flow rates are easily 20 times higher near the Polar apogee than they are near perigee, although the larger content of summer-time data in the northern hemisphere does add an upward bias of the order of 30% (cf. Figure 2). Taking that into account, then a 20-fold increase in the O^+ energy flow rate from perigee to apogee becomes an approximate upper limit instead, one that applies rather well to the highest

flow rates. It may be noted from the left panels in Figure 6 that the peak O^+ energy flow rate (above 55° latitude and with negative B_z) is about 1.5×10^{26} keV s^{-1} or 24 GW.

The slope of the O^+ number flow rate as function of S is initially steeper in Figure 6 than in Figure 4. This difference is not necessarily due to more efficient transfer of electromagnetic power to the O^+ at higher altitude, but is very likely a sampling bias adding to the effect of increasing S. At these high altitudes, the Polar satellite does not merely traverse the ion flows at large angle and great speed, but may sample different flow paths, or one and the same path for varying length of time, in accordance with varying IMF conditions, for example, conditions that are also defining the values of S.

That varying spatial distribution of flows does have important effects on sampling at these altitudes becomes evident from the behavior of the H^+ ions in Figure 7. Having a dominant component of solar wind-origin H^+ ions, the northern hemispheric H^+ flow rates ought to be especially well correlated, loosely speaking, with the solar wind kinetic energy flow density K, which is the product of solar wind number flow density and mean ion energy. However, the result of averaging intense inward (earthward) flow in the central cusp with (less intense) outward flow elsewhere hinges on the average orientation of the ion flow paths with respect to the Polar orbit. In Figure 7, upper left panel, negative IMF B_z yields the cleanest positive response of the flow rate (solid lines) to increasing K (circular data symbols are obscured). This case presumably involves the Polar satellite spending a great deal of time immersed in plasma mantle tailward flow. The corresponding increase in mean energy in the bottom left panel (single solid line) is at least superficially consistent with the increase in K being partly due, statistically, to increasing solar wind velocity.

The other three cases in Figure 7 suggest more complex and/or variable orientation of the ion flow paths, especially the sorting by *S* with negative B_z. That case, the only one with a negative slope on the flow rate, illustrates the hazards of averaging inward and outward H^+ flow samplings in and about the cusp region, within a fixed latitude-longitude grid. It reflects a growing weight being assigned to earthward (negative) flow samplings with increasing *S*, at the expense of outward flow, probably associated with equatorward displacement of the cusp by an increasingly negative B_z.

Table 2 sets Figures 6 and 7 in the same kind of context as Table 1, using the same format and again specifically referring to the O^+ data. Despite the very different appearance of the H^+ data themselves, the associated table is nearly identical, since the H^+ and O^+ data are always obtained simultaneously (save for gaps in telemetry), and the data selection is based on the same IMF and solar wind conditions. The flow density samplings are much more numerous here, 12 to 17 times more, and consist mostly of 24-second averages. Apart from that and the larger average radial distance, about 7.5 R_E, this table contains very nearly the same numbers as Table 1, confirming that the northern and southern sets of hemispheric outflow rates were observed under essentially identical solar wind conditions, as intended.

Figure 8 is an attempt to extract ionosphere-origin H^+ flows from the near-apogee samplings by only accepting magnetic footprints inferred to be on the night-side of the Magnetic Pole. Note that the flow rate scale is one-tenth of that in Figure 7 and the same as that for O^+ ions in Figure 6. Note also that these rates only refer to the nighttime half of the polar region and therefore probably represent less than half of the hemispheric outward flow of H^+ ions from the ionospheric source (cf. *Yau et al.* [1985b]). A table like the previous two for this figure would

have about half the number of samplings in Table 2 but would be virtually identical otherwise (not shown).

6. Discussion

6.1. Margins of Error

The only kind of error that we are able to ascertain with a high degree of confidence is the one resulting specifically from counting statistics, assuming standard Poisson statistics. Having kept careful log of the propagation of variances through our mathematical operations, we conclude that this kind is negligible. Specifically, the relative counting errors on the hemispheric ion number flow rates are in most cases of the order of 0.1% or less, even when the flow density samplings are each admitted with a 100% cap on relative standard deviation. The reason for the small final errors is two-fold: (*i*) The number of samplings is large, and (*ii*) each sampling is itself a sum of terms (Equation 1) that together represent the cumulative exposure of a large instrument geometric factor (as much as 0.05 cm^2 sr per detector half, depending on energy; cf. *Shelley et al.* [1995]) to ions for at least 8 seconds (effective recording time during two spin cycles).

The large statistical material notwithstanding, the binning of our measurements in latitude and longitude does introduce a non-negligible margin of error, the reason being the extremely large dynamic range of individual flow densities. This effect is intertwined with the issue of unidirectional versus bi-directional flow density samplings (Section 2.5). Based on extensive experimentation with different grids, we estimate that when adding samplings of both signs (outward and inward), the grid-related numerical scatter is typically well within 10%, plus or minus, with respect to hemispherical integration for the O^+, but it can exceed that limit. A fairly

conservative upper limit on this numerical uncertainty is ±20%. The situation with the H^+ is more complicated, because of the strongly bi-directional nature of solar wind-origin flows near apogee, but a 20% margin does apply to near-perigee outward flow rates of H^+ ions as well. The mean energies, by our estimate, have somewhat larger grid-related uncertainty, about ±30%.

These ±20% and ±30% arithmetic margins, we believe, also account for the uncertainties in assigning nominal "magnetic footprints", or more generally speaking, assigning near-Earth points of origin of the measured ions. Besides using simplified footprints (from MFE Key Parameters), we have entirely neglected cross-field ion drifts. The fastest form of drift, **E×B** drift, is certainly capable of shifting the apparent footprint a significant distance, especially with the lowest-energy O^+ ions (see e.g. *Delcourt et al*. [1988 and 1989]). Even with typical ion transit times of the order of 10 minutes or less from the "point of acceleration" (Section 3), a transverse electric field of, say, 0.1 Vm^{-1} at $R \sim 2\ R_E$ could, in principle, displace an ion's conjugate footprint some 30° in latitude over the course of 10 minutes. That would change, quite significantly, the multiplier used for entering the corresponding flow density sampling in the average hemispheric outflow rate. However, electric fields that strong are localized [e.g. *Mozer et al.*, 1977], and the **E×B** drift tends to average out across an entire polar region. As a consequence, drift-related arithmetic errors are in fact already part of the scatter we found by using different grids for averaging.

Absolute calibration of an instrument as "multi-dimensional" as TIMAS involves a great deal of interpolation between known calibration points. We are nevertheless reasonably confident that our calibration is on the whole accurate to within about 30% with O^+, H^+ and He^+ data included here (obtained before December 9, 1998), provided their signal-to-background ratio is substantially greater than one. It may actually be somewhat better, considering the rather good

agreement we have found in flight with positive-ion spectra from the Polar HYDRA instrument [*Scudder et al.*, 1995] when H^+ ions dominate. We cannot make the same claim with respect to He^{++} data, however, at least not in the cusp regions, where intense H^+ count rates interfere with the H^+ versus He^{++} anode positioning in ways that were not anticipated and therefore not calibrated prior to flight. The latter is the reason for omitting displays of He^{++}/H^+ ratios here, so as not to overburden the presentation with caveats.

Sorting our flow density samplings by the solar wind plasma and magnetic field WIND Key Parameters, including time shifting, expands these margins of error in ways that are difficult to estimate even by experimentation. For the most part we have treated the energy flow densities K and S, derived with Equations 5 and 6, as exact numbers, only requiring that both plasma and IMF parameters be available simultaneously. However, we did discover, by some experimenting, that the derivation of S is prone to produce occasional values that are almost certainly much too large, presumably due to faulty IMF parameters (which enter in squared form). By our excluding such samplings (110 total, each associated with 15 minutes of IMF data), the various dynamic ranges of S appearing in Figures 4 through 8 were reduced by between 1% and 9% (separate ±99 nT caps were applied to the IMF B_z). The associated effects on the average flow rates were much less than 1%. For a quantitative analysis of error margins on time shifting, including the effects of having the solar wind monitor located at varying distance from the Sun-Earth line, see for example *Collier et al*. [1998].

6.2. Interpretation

6.2.1. Altitude variation of ion outflow rates. As illustrated by Figures 2, 4 and 5, the TIMAS instrument finds generally weaker H^+ than O^+ outflow rates near the Polar perigee, at R

≈ 2 R_E, in the 1996-98 time period, which begins about solar minimum. This is unexpected, because the extensive long-term statistics previously provided by the EICS ion mass spectrometer on the DE-1 satellite [*Yau et al*., 1985a and b], covering the rather similar energy range of 10-eV/e to 17-keV/e, would suggest the opposite to be true during this phase of the solar cycle. More specifically, the H^+ outflow rate would be expected to be as much as two to three times higher than the O^+ rate during geomagnetically quiet conditions, whereas the two rates might be comparable during active conditions, due to the stronger activity-related O^+ increase (see e.g. page 75 in *Hultqvist et al*. [1999]).

This seeming discrepancy is discussed by *Peterson et al*. [2001], who argue that it probably is due to the different altitudes of the observations. That is, the DE-1 observations, having been made at geocentric $R \sim 2.5$ to 4.5 R_E, are likely to show the effects of continued acceleration of H^+ ions well above 2 R_E, including the acceleration of less-than-10 eV H^+ into the EICS energy range. Indirect support for this interpretation is provided with the help of "suprathermal" ion data from the Akebono satellite by *Cully et al.* [2003], who find that the <10 eV H^+ outflow rate at $R \sim 2$ R_E is well sufficient to supply the H^+ ions observed at DE-1. Being able to show TIMAS hemispheric outflow rates from $R \sim 4$ to 9 R_E here, we should be able to settle this issue once and for all, it seems. The results are inconclusive, however.

By comparing the coloration of normalized Ḣflow densities in the southern and northern auroral zones in Figure 1, taking into account the different color bars and excluding the cusp surroundings, it is clear that the H^+ ions above the nominal 15 eV threshold have become much more numerous at the northern high altitudes. The average auroral-zone flow density appears to be about 10^{12} $m^{-2}s^{-1}$ in the North (normalized to 300 km altitude) versus only 10^{11} $m^{-2}s^{-1}$, or maybe slightly more, in the South. Hence, there is an almost 10-fold increase in the H^+ outward

number flow rate with altitude in this part of the auroral zone, and that is more than the corresponding increase in the O^+ rate. In fact, the normalized flow density of the O^+ ions in Figure 1, within the same parts of the auroral zones, seems to be of the order of 10^{11} $m^{-2}s^{-1}$ in both the North and South (note the different color bars). On the other hand, the O^+ flow density within the northern polar cap has increased significantly over its southern counterpart, and a major portion of the O^+ outflow originates in and around the cusp projection on the ionosphere, a region that defies a North-South comparison for the ionospheric H^+ ions. In terms of hemispheric rates, the O^+ outflow is also larger near apogee, by a factor of at least 2.5, according to Figure 2. All that can be concluded from these comparisons is that the Peterson et al. interpretation may well be true, allowing for the unknown ionosphere-origin portion of the cusp-related H^+ flow. Figure 8 does not resolve the issue, of course, but it does show that the northern night-side flow rate alone is two to five times higher than the entire southern H^+ outward flow rate in Figure 5.

6.2.2. Slow time variation of O^+ outflow rate. Returning to Figure 2, we note two slow trends in the O^+ flow rate, namely a gradual increase over time (1996-98) and a seasonal oscillation with greater flow during the local summer half of the year. Both are qualitatively consistent with the DE-1 results of *Yau et al.* [1985a and b] and with the interpretation by these and other authors [*Young et al*., 1982]: (*i*) The O^+ rate of outflow increases with increasing solar activity, essentially because the associated increase in solar EUV radiation raises the O^+ scale height in the topside ionosphere, feeding more of these ions into the high-altitude acceleration region, and (*ii*) the summer-time hemisphere receives more solar irradiation. The O^+ seasonal oscillation is less obvious in the southern hemisphere statistics of *Peterson et al.* [2001], possibly because of their different computational methods. Rather than applying Equation 1 above directly to the differential flux arrays, they have used a more circuitous method of combining

previously calculated number densities and mean velocity vectors, which may have enlarged the scatter from rounding errors.

In Figure 2, however, we also note a strong seasonal similarity between the northern and southern O^+ flow rates, on the one hand, and the northern, near-apogee flow rate of H^+ ions, on the other. Since the latter is almost certainly dominated by solar wind-origin ions, and since flow rates in this figure, as mentioned before, are derived from samplings with flow density away from Earth (or otherwise set to zero), this H^+ rate must reflect an actual seasonal variation of the inflow of magnetosheath plasma through the northern cusp (observations made at $R \leq 9$ R_E, well inside the magnetopause), the inflow peaking during the summer half of each year. That is not likely to be controlled by solar EUV radiation, but it might well result from the seasonal variation of the daily average tilt angle of Earth's magnetic dipole with respect to the solar wind flow direction. In other words, the northern cusp lets more magnetosheath plasma through during the northern summer, when it is tilted more directly into the oncoming sheath flow. This has in fact been postulated before by *Newell and Meng* [1988], based on their observation of hemispherical asymmetry in cusp precipitation at 800 km altitude near solstices, mainly with respect to the low-energy portion of the magnetosheath plasma. This effect may in turn modulate the O^+ outflow rate in addition to the effects of a varying daily dose of EUV, not necessarily by raising the O^+ scale height, but quite possibly by influencing the high-altitude acceleration mechanism.

6.2.3. Kinetic versus electromagnetic solar wind control. From Figures 4 and 5 it is obvious that the ionospheric outward flow rates do increase monotonically with increasing *K* or *S*, especially strongly in the case of O^+ ions, but there are some subtle differences suggesting that *K* is the more essential input. Consider first the positive IMF B_z case: The dynamic range of *K*,

counted as the ratio between the right and left extremes, is 9.4. The similar range of *S* is almost 11, that is somewhat larger. Yet, the corresponding increases in the O^+ outflow rate (Figure 4) at greater than 55° latitude, for instance, are a factor of 9.3 with *K*, almost proportional, versus a factor of only 4.5 with *S*. The corresponding numbers for the H^+ outflow rate (Figure 5) are 5.6 with *K* and a mere 1.8 with *S*. Then consider the negative B_z case: The dynamic ranges are 7.5 for *K* and a little over 10 for *S*, and the increases in the O^+ outflow rate are 5.7 with *K* and 5.0 with *S*, whereas the increases in the H^+ rate are 2.6 with *K* and 1.6 with *S*.

Hence, four statistically independent comparisons, that is with positive and negative B_z, and each with both O^+ and H^+, all suggest the same trend: an approximately 8- to 9-fold increase in *K* produces a greater increase in ion outflow rate than does a 10- to 11-fold increase in *S*. To some extent, Table 1 allows for simultaneous comparison with *K* and *S*: For example, in the upper left group of parameters, with negative B_z and with *K* the ordering parameter, the associated average energy flux *S* increases 20% between the left and middle columns, and yet the corresponding O^+ flow rates in Figure 4 (upper left panel, solid lines) increase about 50%, apparently in response to the factor 2.3 increase in *K*. On the other hand, in the opposite corner of Table 1, with positive B_z and with *S* the ordering parameter, the increase in average *K* is only a factor 1.7 from middle to right column, probably too little to fully explain the corresponding tripling of the O^+ flow rates in Figure 4 (upper right panel, dashed lines). In this case, at least, the quadrupling of *S* may indeed contribute, possibly indirectly, via the effects of increasing IMF B_y and B_z on nightside substorm activity.

Setting B_z = 3 nT and B_y = 0 in Equation 6 and noting that the solar wind speed is usually greater than 300 km s^{-1}, we obtain a practical low-end limit on *S* of about 2 _Wm^{-2}. This is indeed reflected in the lowermost *S* coordinate in Figures 4 through 8 but has no important

implications for the preceding analysis. With reference to the right half of Table 1, for instance, specifically to the third columns from right, the minimum binned average S of 6 with both $B_z <$ −3 nT and $B_z >$ +3 nT is changed to 4 _Wm^{-2} (rounded) if the processing is redone with the less restrictive conditions that B_z be merely all negative or all positive. The other four S values in the columns to the right are then also changed slightly, and the net result is circa 50% increase in the dynamic range of binned S. Any low-end limit on acceptable samplings of S also means an implied low-end limit on K, because K is virtually always at least an order of magnitude greater than S (cf. Tables 1 and 2), that is at least about 20 _Wm^{-2} in the preceding analysis, roughly speaking. This, however, is too small, typically corresponding to a solar wind density of less than 1 cm^{-3}, to have a significant impact on the average K below 300 _Wm^{-2}, as confirmed by reprocessing with merely negative or positive B_z. If we use those reprocessed data (not illustrated) for the O^+, for example, the above kind of comparison between the flow rate dependencies on K and S gives the following numbers for southern outflow:

In the case of IMF$B_z >$ 0, the dynamic range of K, again counted as the ratio between the highest and lowest bin averages, is now 8.5, while the similar range of S has increased to 16.4. Yet, the corresponding dynamic ranges of the O^+ outflow rate above 55° latitude are now a factor of 7.5 with K versus a factor of 4.2 with S. In the $B_z <$ 0 case, the dynamic ranges are 7.6 for K and 15.7 for S, and the ranges of the O^+ outflow rate are as large as 9.4 with K while only 6.6 with S. Hence, a circa 8-fold increase in K still produces a significantly greater increase in the near-perigee O^+ outflow rate than does even a 16-fold increase in S.

This kind of comparison cannot be made in a statistically unbiased fashion for near-apogee flow rates, however. Unlike the near-perigee samplings, which are all made while the Polar satellite is essentially traversing the outward flow vectors at right angle, regardless of K and S,

many of the samplings near apogee are made while the satellite is moving nearly parallel or anti-parallel to the ion flow, causing over-sampling of one and the same set of conditions, and those conditions include *K* and *S* in ways that are difficult to quantify.

7. Summary and Conclusions

We may interpret Figure 2 as showing that the extraction of O^+ ions from the topside ionosphere and their acceleration to energies within the 15-eV to 33-keV range are to a significant degree controlled by the varying inflow of magnetosheath plasma in the cusps, this inflow manifested by the northern hemisphere H^+ flow rates. That interpretation is also consistent with the locally enhanced O^+ flow density in the cusp regions of Figure 1, and it meshes quite well, in fact, with earlier reports on the outflow of O^+ ions with energies below 15 eV, since the rate of outflow of so called "suprathermal" O^+ ions has been found to be especially strong in the cusp regions ("ion fountains"; *Lockwood et al.* [1985]) and rather well correlated with the solar wind dynamic pressure, especially with its standard deviation, more so than with several other solar wind parameters [e.g. *Moore et al*., 1999; *Elliott et al*., 2001; *Cully et al*., 2003]. In terms of solar wind power input, it might seem then that the kinetic energy flow density *K* ought to be especially important, a conjecture that can indeed be drawn from the above comparison of *K* and *S* in Figures 4 and 5, as well. The latter applies to both the O^+ and the H^+ outflows, although the H^+ flow rate varies less in absolute numbers.

Figures 4 and 6 together suggest that the transfer of energy to the O^+ ions takes place over a large range of altitude, that is over several Earth radii. Specifically, the combined increases in mean energy and number flow rate, if the latter is discounted by 30% to compensate for the larger fraction of summertime samplings near the Polar apogee (Figure 2), imply a 20-fold

increase in the peak O^+ energy flow rate (at maximum K and negative B_z) from perigee altitude. The increase in number flow rate alone implies either of two scenarios: (*i*) Ions are accelerated continually and at greatly varying rates, with a majority reaching energies above 15 eV (plus s/c potential) only at very high altitude, or (*ii*) below-15-eV ions may become randomly accelerated at any of a large range of altitudes.

The first scenario brings to mind the concept of centrifugal acceleration along curved magnetic field lines under **E×B** drift [*Cladis*, 1986], but the observed near-apogee mean O^+ energy of between one and two keV is probably too large for that kind of explanation. A single event analyzed by *Cladis et al*. [2000], with data from the TIMAS instrument, was indeed found to be consistent with rapid (2 minutes) centrifugal acceleration of O^+ ions to about one keV near the Polar apogee, but that event involved unusually strong and rapid compression of the magnetosphere. Under more normal and near-steady conditions the centrifugal acceleration is not expected to generate keV energies until the ions reach the strongly curved portion of field lines at the tail mid-plane (see Figure 2 in *Cladis* [1986]; see also *Delcourt et al.* [1988 and 1989]). Furthermore, this mechanism by itself generates field-aligned velocity distributions, whereas the TIMAS observations very often show broad pitch-angle distributions of up-flowing ions at all altitudes [*Lennartsson*, 2003].

Alternatively, one might envision cumulative transverse ion "heating" by plasma waves [e.g. *Retterer et al*., 1983]. That would seem to allow for greatly varying acceleration rates as well as broad ion pitch-angle distributions. In fact, it is a vision that has been prompted by the frequent observations over the last 30 years of transversely accelerated ions, and it is one that is specifically consistent, superficially at least, with published statistics on the altitude dependence of "conical" ion velocity distributions [e.g. *Peterson et al.*, 1992; *Miyake et al.*, 1993 and 1996].

However, a smoothly progressing form of acceleration alone cannot explain the occasional observation [*Lennartsson*, 2003] of azimuthally collimated and monoenergetic keV O^+ ions at 90° pitch angle at high altitude ($R \sim 6\ R_E$).

The second scenario requires an acceleration mechanism that is random in both time of onset and location, where "location" may mean multiple narrow-scale sites. Such a mechanism may involve both transverse ion acceleration, creating "newly born conics" in the parlance of *Miyake et al.* [1993], and the parallel kind. A random-type, narrow-scale (filaments) mechanism to fit that mold is outlined in *Lennartsson* [2003], although its specific purpose is to help explain the collocation of transversely accelerated H^+, He^+ and O^+ ions with transient bursts of hot H^+ ions from the near-midnight tail, rather than with cusp ion bursts. This mechanism would be powered by the kinetic energy flux associated with the H^+ bursts (and with accompanying electrons). The growing mean energy of the up-flowing O^+ ions in that case might well be due in large part to increasing efficiency of the mechanism itself (growing size of the hot-H^+ gyro radii with altitude).

Whereas the solar wind*K* only carries kinetic power per se, the polarity of the IMF B_z does make a visible difference in all of Figures 2 through 8. The difference is the largest in Figure 4, where the O^+ flow rate is mostly three times greater with negative B_z. This is significantly more of a difference than previously reported about both polar region O^+ outflows in various energy ranges [e.g. *Abe et al*., 1996; *Øieroset et al*., 2000; *Elliott et al*., 2001; *Cully et al*., 2003] and the 0.1- to 16-keV O^+ concentration in the plasma sheet [*Lennartsson*, 1995]. The larger difference may be caused by a combination of two circumstances: (*i*) The ± 3 nT or stronger B_z is a more discerning condition than most previously used, and (*ii*) the 15-minute averaging may be a fortuitous choice. In any case, the modulation by the IMF B_z does not necessarily diminish the

role of the solar wind kinetic energy flux, since a negative B_z may serve both to enhance the concurrent influx of magnetosheath plasma through the cusps (cf. Figure 2) and to induce the release of previously stored solar wind-origin kinetic energy from the tail (hot plasma bursts) during substorms and magnetic storms.

Appendix

A1. The TIMAS Instrument

TheToroidal Imaging Mass-Angle Spectrograph, or TIMAS [*Shelley et al*., 1995], combines magnetic mass analysis with simultaneous recording of all species (all M/Q) and a nearly spherical field of view. This is accomplished by accepting ions within a 10° by nearly 360° wide window, centered on a cone of 73° half-angle, and, following the energy selection, magnetically dispersing them in the radial direction on a large annular detector (MCP) with position-sensitive anode. Allowing a cone-shaped field of view, as opposed to a planar one (at 90°), enables the optimal internal focusing of the ion trajectories without the addition of complex external deflectors. Since the axis of the cone is perpendicular to the Polar spin axis, the total field of view scanned over the course of each 6-second spin cycle is nevertheless as much as 98% of the full 4π. A grossly three-dimensional sampling is achieved after only half a spin (3 s) by a combination of 28 detector sectors, but it takes a full spin to fill in gaps in the angular coverage with the help of an elevation phase shift between the leading and trailing sets of 14 sectors each.

The full energy range is 15 eV/e (above s/c potential) to 33 keV/e, covered in 28 channels, of which the 14 even-numbered channels are used on even-numbered spins, and the 14 odd-numbered ones on odd spins. Each set of 14 channels is swept 16 times per spin. Hence, the time to sample essentially the entire energy-angle space available for each ion species is 6 seconds (or

3 s with angular gaps), but it takes 12 seconds (2 spins) to fill in the interleaving energy channels. The instrument is operated in essentially a fixed cycle, continually processing the ion counts into various mass-energy-angle arrays and returning, within the limitations of available telemetry, the same set of arrays, according to a commanded priority order.

The principal data arrays are 6-second (single-spin) energy distributions in each of 208 partially overlapping solid angles (approx. 22.5° by 22.5° each) for each major ion, all corrected by subtraction of separately monitored detector background counts. For the sake of calculating velocity moments, as done in the present study, these arrays are combined into 12-second and 28-energy pairs (or 24-s groups of four, depending on altitude). All arrays are operationally subdivided into two independently commanded parts, one part from each independently powered half of the detector. In the case of the present statistical study, most of the relevant data have been collected with only one of the two detector halves, the one always telemetered at full energy resolution. Therefore, the angular coverage is slightly reduced from optimal and requires a wider solid-angle extrapolation near one of the two spin axis directions (due to the asymmetric detector mounting). However, since the spin axis is perpendicular to the Polar orbital plane, this direction is normally at large angle to the magnetic field (near 90°), so the effect on the calculation and averaging of magnetic field-aligned ion flows is probably a minor one. Final pitch angles are calculated during ground data processing with magnetic field information from the Polar MFI instrument [*Russell et al*., 1995].

A2. Detector Background Subtraction

The TIMAS instrument, like the earlier generation mass spectrometers, monitors detector background radiation counts (mostly due to bremsstrahlung from MeV radiation belt electrons)

by periodically setting analyzer voltages to exclude all ambient plasma, specifically once per energy sweep. The subtraction of this background noise from the nominal signal during ground data processing is considerably more involved, however, because of the TIMAS imaging. The noise is traced to any of the 28 detector sectors, but its radial position is recorded at a much coarser resolution than is that of the ions, namely by four radial bands, as compared with 64 radial bins for the ions, and each of the 28 by 4 possible noise rates is only telemetered as a 6-second sum over spin angle.

This arrangement is hardwired and intended to lessen the burden on both the telemetry and the instrument processor. Assuming that the noise rates have indeed remained constant in time for six seconds, despite the turning of the instrument, the background to be associated with a given M/Q then still needs to be derived via radial interpolation and proportioning, a procedure that could not be pre-flight calibrated within available resources. Complicating matters further is the fact that each ion image, typically spanning 3 or 4 of the 64 radial bins, has to be allowed to move (in a calibrated fashion) with ion energy (given the electric power limitations), whereas any non-uniformity in the background, caused by material structures in the satellite or in the instrument itself, is likely to be fixed in radial position. As a consequence, the TIMAS background subtraction is subject to possible unknown errors beyond pure counting statistics, and these pose a problem when the signal-to-noise ratio is small (of the order one or smaller). For this study, data with more than 1000 background counts per 6-second spin, i.e. in about 0.3 seconds of cumulative background sampling, are excluded from all averages displayed. This represents a few percent of all data.

A3. Solar Wind Time Shifting

Solar wind plasma and magnetic field Key Parameters used here have been time shifted by an iterative method along the Sun-Earth line (~ bulk flow vector), assuming that gradients in the perpendicular directions are negligible within the range of the solar wind monitor. As a simplified example, assuming that at time t the WIND monitor is positioned near the L1 Lagrangian point, at say GSE x = 230 R_E, and shows a solar wind speed of $v(t)$, pressure $p(t)$ and magnetic field $\mathbf{B}(t)$. Based on these starting values for v, p and $\mathbf{B}$, the positions of Earth's bow shock and magnetopause are predicted from the empirical model of *Petrinec and Russell* [1996], followed by the calculation of the distances $\_x$ between WIND and the subsolar bow shock and $\_x$ between the bow shock and the magnetopause and a corresponding flight time of $\_t = \_x / v(t) + \_x / v'(t)$, assigning a reduced speed v' between bow shock and magnetopause (by factor 1/4). A new set of v, p and $\mathbf{B}$ is then obtained from WIND data taken at time $t - \_t$, and this set is used to infer a new $\_t$, etc. This iteration is repeated a maximum of four times (beyond the starting values), or it is ended if two consecutive $\_t$ values (about 1 h each in this example) differ by less than 1% (the normal case). The actual iteration is slightly more complex in that each $\_t$ is based on (typically) five adjacent WIND measurements of the bulk velocity v, and the same $\_t$ is used over some extended length of time, contingent on the stability of the WIND measurements.

Acknowledgments. This work was supported by NASA under grant NAG5-12857 and contract NAS5-30302.

References

Abe, T., S. Watanabe, B.A. Whalen, A.W. Yau, and E. Sagawa, Observations of polar wind and thermal ion outflow by Akebono/SMS, *J. Geomag. Geoelectr., 48*, 319,1996.

Cladis, J.B., Parallel acceleration and transport of ions from polar ionosphere to plasma sheet, *Geophys. Res. Lett., 13*, 893, 1986.

Cladis, J.B., H.L. Collin, O.W. Lennartsson, T.E. Moore, W.K. Peterson, and C.T. Russell, Observations of centrifugal acceleration during compression of magnetosphere, *Geophys. Res. Lett., 27*, 915, 2000.

Collier, M.R., J.A. Slavin, R.P. Lepping, A. Szabo, and K. Ogilvie, Timing accuracy for the simple planar propagation of magnetic field structures in the solar wind, *Geophys. Res. Lett., 25*, 2509, 1998.

Collin, H.L., R.D. Sharp, E.G. Shelley, and R.G. Johnson, Some general characteristics of upflowing ion beams over the auroral zone and their relationship to auroral electrons, *J. Geophys. Res., 86*, 6820, 1981.

Cully, C.M., E.F. Donovan, A.W. Yau, and G.G. Arkos, Akebono/suprathermal mass spectrometer observations of low-energy ion outflow: Dependence on magnetic activity and solar wind conditions, *J. Geophys. Res., 108*, 1093, 2003.

Delcourt, D.C., J.L. Horwitz, and K.R. Swinney, Influence of the interplanetary magnetic field orientation on polar cap ion trajectories: Energy gain and drift effects, *J. Geophys. Res., 93*, 7565, 1988.

Delcourt, D.C., C.R. Chappell, T.E. Moore, and J.H. Waite Jr., A three-dimensional numerical model of ionospheric plasma in the magnetosphere, *J. Geophys. Res., 94*, 11,893, 1989.

Elliott, H.A., R.H. Comfort, P.D. Craven, M.O. Chandler, and T.E. Moore, Solar wind influence on the oxygen content of ion outflow in the high-altitude polar cap during solar minimum conditions, *J. Geophys. Res., 106*, 6067, 2001.

Ghielmetti, A.G., R.G. Johnson, R.D. Sharp, and E.G. Shelley, The latitudinal, diurnal, and altitudinal distributions of upward flowing energetic ions of ionospheric origin, *Geophys. Res. Lett., 5*, 59, 1978.

Hultqvist, B., M. Øieroset, G. Paschmann, and R. Treumann (Eds.), *Magnetospheric Plasma Sources and Losses*, Kluwer Academic Publishers, Dordrecht, pp. 7-84, 1999.

Lennartsson, O.W., Statistical investigation of IMF B_z effects on energetic (0.1- to 16-keV) magnetospheric O^+ ions, *J. Geophys. Res., 100*, 23,621, 1995.

Lennartsson, O.W., In situ Polar observation of transverse cold-ion acceleration: Evidence that electric field generation is a hot-ion finite gyroradii effect, *J. Geophys. Res., 108*, 1152, 2003.

Lennartsson, W., and E.G. Shelley, Survey of 0.1- to 16-keV/e plasma sheet ion composition, *J. Geophys. Res., 91,*, 3061, 1986.

Lennartsson, O.W., K.J. Trattner, H.L. Collin, and W.K. Peterson, Polar/Toroidal Imaging Mass-Angle Spectrograph survey of earthward field-aligned proton flows from the near-midnight tail, *J. Geophys. Res., 106*, 5859, 2001.

Lepping, R.P., *et al.*, The WIND magnetic field investigation, in *The Global Geospace Mission*, ed. by C.T. Russell, Kluwer Academic Publishers, Dordrecht, 207, 1995.

Lockwood, M., M.O. Chandler, J.L. Horwitz, J.H. Waite, Jr., T.E. Moore, and C.R. Chappell, The cleft ion fountain, *J. Geophys. Res., 90*, 9736, 1985.

Lundin, R., B. Hultqvist, N. Pissarenko, and A. Zacharov, Composition of the hot magnetospheric plasma as observed with the PROGNOZ-7 satellite, in *Energetic Ion*

Composition in the Earth's Magnetosphere, ed. by R.G. Johnson, Terra Scientific Publishing Co., Tokyo, Japan, 307, 1983.

Miyake, W., T. Mukai, and N. Kaya, On the evolution of ion conics along the field line from EXOS D observations, *J. Geophys. Res., 98*, 11,127, 1993.

Miyake, W., T. Mukai, and N. Kaya, On the origins of the upward shift of elevated (bimodal) ion conics in velocity space, *J. Geophys. Res., 101*, 26,961, 1996.

Moore, T.E., W.K. Peterson, C.T. Russell, M.O. Chandler, M.R. Collier, H.L. Collin, P.D. Craven, R. Fitzenreiter, B.L. Giles, and C.J. Pollock, Ionospheric mass ejection in response to a CME, *Geophys. Res. Lett., 26*, 2339, 1999.

Mozer, F.S., N.K. Hudson, R.B. Torbert, B. Parady, and J. Yatteau, Observations of paired electrostatic shocks in the polar magnetosphere, *Phys. Rev. Lett., 38*, 292, 1977.

Newell, P.T., and C.-I. Meng, Hemispherical asymmetry in cusp precipitation near solstices, *J. Geophys. Res., 93*, 2643, 1988.

Ogilvie, K.W., *et al.*, SWE, a comprehensive plasma instrument for the WIND spacecraft, , in *The Global Geospace Mission*, ed. by C.T. Russell, Kluwer Academic Publishers, Dordrecht, 55, 1995.

Øieroset, M., M. Yamauchi, L. Liszka, and S.P. Christon, Energetic ion outflow from the dayside ionosphere and its relationship to the interplanetary magnetic field and substorm activity, *J. Atmos. Solar-Terr. Phys., 62*, 485, 2000.

Peterson, W.K., H.L. Collin, M.F. Doherty, and C.M. Bjorklund, O^+ and He^+ restricted and extended (bi-modal) ion conic distributions, *Geophys. Res. Lett., 19*, 1439, 1992.

Peterson, W.K., H.L. Collin, A.W. Yau, and O.W. Lennartsson, Polar/Toroidal Imaging Mass-Angle Spectrograph observations of suprathermal ion outflow during solar minimum conditions, *J. Geophys. Res., 106*, 6059, 2001.

Petrinec, S.M., and C.T. Russell, Near-Earth magnetotail shape and size as determined from the magnetopause flaring angle, *J. Geophys. Res., 101*, 137, 1996.

Pollock, C.J., M.O. Chandler, T.E. Moore, J.H. Waite, Jr., C.R. Chappell, and D.A. Gurnett, A survey of upwelling ion event characteristics, *J. Geophys. Res., 95*, 18,969, 1990.

Rème, H., *et al.*, First multispacecraft ion measurements in and near the Earth's magnetosphere with the identical Cluster ion spectrometry (CIS) experiment, *Ann. Geophysicae, 19*, 1303, 2001.

Retterer, J.M., T. Chang, and J.R. Jasperse, Ion acceleration in the supraurоral region: A Monte Carlo model, *Geophys. Res. Lett., 10*, 583, 1983.

Russell, C.T., *et al*., The GGS/Polar magnetic fields investigation, in *The Global Geospace Mission*, ed. by C.T. Russell, Kluwer Academic Publishers, Dordrecht, 563, 1995.

Scudder, J., *et al*., HYDRA-A 3-dimensional electron and ion hot plasma instrument for the Polar spacecraft of the GGS Mission, in *The Global Geospace Mission*, ed. by C.T. Russell, Kluwer Academic Publishers, Dordrecht, 459, 1995.

Shelley, E.G., D.A. Simpson, T.C. Sanders, E. Hertzberg, H. Balsiger, and A. Ghielmetti, The energetic ion composition spectrometer (EICS) for the Dynamics Explorer-A, *Space Sci. Instrum., 5*, 443, 1981.

Shelley, E.G., *et al*., The toroidal imaging mass-angle spectrograph (TIMAS) for the Polar Mission, in *The Global Geospace Mission*, ed. by C.T. Russell, Kluwer Academic Publishers, Dordrecht, 497, 1995.

Tsyganenko, N.A., Modeling the Earth's magnetospheric magnetic field confined within a realistic magnetopause, *J. Geophys. Res., 100*, 5599, 1995.

Yau, A.W., B.A. Whalen, W.K. Peterson, and E.G. Shelley, Distribution of upflowing ionospheric ions in the high-altitude polar cap and auroral ionosphere, *J. Geophys. Res., 89*, 5507, 1984.

Yau, A.W., P.H. Beckwith, W.K. Peterson, and E.G. Shelley, Long-term (solar cycle) and seasonal variations of upflowing ionospheric ion events at DE 1 altitudes, *J. Geophys. Res., 90*, 6395, 1985a.

Yau, A.W., E.G. Shelley, W.K. Peterson, and L. Lenchyshyn, Energetic auroral and polar ion outflow at DE 1 altitudes: Magnitude, composition, magnetic activity dependence, and long-term variations, *J. Geophys. Res., 90*, 8417, 1985b.

Young, D.T., H. Balsiger, and J. Geiss, Correlations of magnetospheric ion composition with geomagnetic and solar activity, *J. Geophys. Res., 87*, 9077, 1982.

Figure Captions

Figure 1. Normalized (to 300 km alt), binned (in MLT and INVL; see text for details) and color-coded upward ion flow densities above 55° invariant latitude in the southern (bottom) and northern (top) hemispheres. Southern densities have one common color bar (on the right), in units of $m^{-2}s^{-1}$, whereas northern densities have one for the O^+ and He^+ and another for the H^+. Pink color means saturation, gray means lack of samplings.

Figure 2. Seasonal (6 months winter W or summer S) average rates of ion outflow in southern (average R(SM) ≈ 2.2 R_E) and northern (average R(SM) ≈ 7.5 R_E) hemispheres during 1996-98, subdivided by the preceding 15-minute average IMF B_z polarity (in GSM coordinates). Note: Northern H^+ flow rates are dominated by plasma mantle flow.

Figure 3. Extended (33 months) average rates of O^+ outflow in the southern hemisphere above each of three different invariant latitudes (55°, 60° and 65°), while (1) the preceding 15-min average solar wind kinetic energy flow density K is at certain mean levels (see text), and (2) the associated 15-min average IMF B_z is either positive (dashed lines) or negative (solid lines) by more than 3 nT. Left panel is based on strictly outward flow, treating net earthward flow as zero-flow samplings, right panel includes flows of both signs (see text).

Figure 4. Top left: Same as right panel of Figure 3. Top right: Corresponding flow rates when sorted by preceding 15-min average solar wind electromagnetic (Poynting) energy flow density S (see text). Bottom: Corresponding (> 55°) mean energies, defined as outward energy flow rate divided by number flow rate (error bars reflect spread among the three latitudes, see text).

Figure 5. Analogous to Figure 4 but for H^+ ions. Note the different mean-energy scale.

Figure 6. Northern hemisphere counterpart of Figure 4. Note the different scales for both flow rate and mean energy.

Figure 7. Analogous to Figure 6 but for H^+ ions. Note the different flow-rate scale (increased by factor 10).

Figure 8. Similar to Figure 7 but limited to flow with apparent night-side source. Note the reduced scale for flow rate (by factor 1/10).

Table 1. Average Environmental Parameters With Figure 4 for Latitudes Greater Than 55°

	Grouped by Solar Wind K			Grouped by Solar Wind S		
			IMF B_z < −3 nT			
Samples	2672	6948	913	4829	4001	1703
R (R_E)	2.2	2.3	2.3	2.3	2.3	2.2
Kp	2+	3o	5-	2+	3o	5-
Dst	−26	−24	−47	−17	−25	−58
F10.7	100	86	101	88	90	104
IMF B_z (nT)	−5	−5	−7	−4	−5	−9
SW n (cm^{-3})	6	10	20	9	10	12
SW p (nPa)	1	3	7	2	3	4
SW v ($km\ s^{-1}$)	371	413	498	397	412	444
SW K (μWm^{-2})	223	517	1673	445	533	842
SW S (μWm^{-2})	14	17	55	6	17	63
			IMF B_z > +3 nT			
Samples	2345	5142	705	3366	3544	1282
R (R_E)	2.2	2.3	2.1	2.3	2.2	2.2
Kp	1o	2-	3o	1+	2-	2+
Dst	−10	−8	−5	−6	−9	−10
F10.7	100	91	89	89	95	99
IMF B_z (nT)	+5	+5	+7	+4	+5	+9
SW n (cm^{-3})	6	11	24	10	10	14
SW p (nPa)	1	3	8	2	3	4
SW v ($km\ s^{-1}$)	371	402	449	381	403	423
SW K (μWm^{-2})	220	526	2072	493	528	899
SW S (μWm^{-2})	13	19	53	6	17	65

Table 2. Average Environmental Parameters With Figure 6 for Latitudes Greater Than 55°

	Grouped by Solar Wind K			Grouped by Solar Wind S		
			IMF B_z < −3 nT			
Samples	33366	87240	13452	58755	53357	21946
R (R_E)	7.5	7.5	7.5	7.4	7.5	7.4
Kp	2+	3o	5-	2+	3+	5-
Dst	−27	−25	−37	−17	−26	−56
F10.7	100	92	99	91	96	104
IMF B_z (nT)	−5	−5	−7	−4	−5	−9
SW n (cm^{-3})	5	10	19	9	10	12
SW p (nPa)	1	3	7	2	3	4
SW v ($km\ s^{-1}$)	380	414	482	393	417	455
SW K (μWm^{-2})	214	526	1614	431	556	897
SW S (μWm^{-2})	17	18	47	7	17	69
			IMF B_z > +3 nT			
Samples	31157	71996	12072	47370	46107	21751
R (R_E)	7.6	7.5	7.6	7.6	7.6	7.6
Kp	1o	2-	3+	1+	2-	3-
Dst	−14	−10	−15	−8	−11	−21
F10.7	104	93	100	94	97	100
IMF B_z (nT)	+5	+5	+8	+4	+5	+9
SW n (cm^{-3})	6	10	20	9	10	12
SW p (nPa)	1	3	7	2	3	4
SW v ($km\ s^{-1}$)	376	407	475	384	410	443
SW K (μWm^{-2})	225	526	1648	410	549	913
SW S (μWm^{-2})	16	18	63	6	17	67

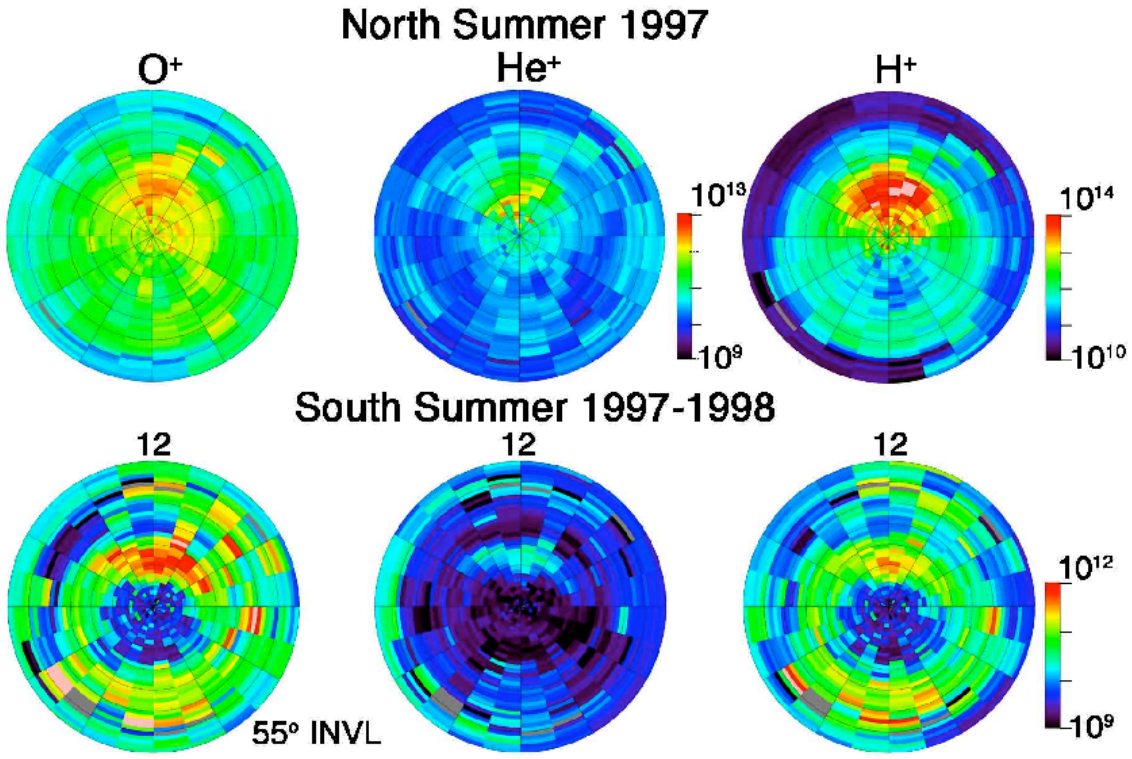

Figure 1. Normalized (to 300 km alt), binned (in MLT and INVL; see text for details) and color-coded upward ion flow densities above 55ϒinvariant latitude in the southern (bottom) and northern (top) hemispheres. Southern densities have one common color bar (on the right), in units of $m^{-2}s^{-1}$, whereas northern densities have one for the O^+ and He^+ and another for the H^+. Pink color means saturation, gray means lack of samplings.

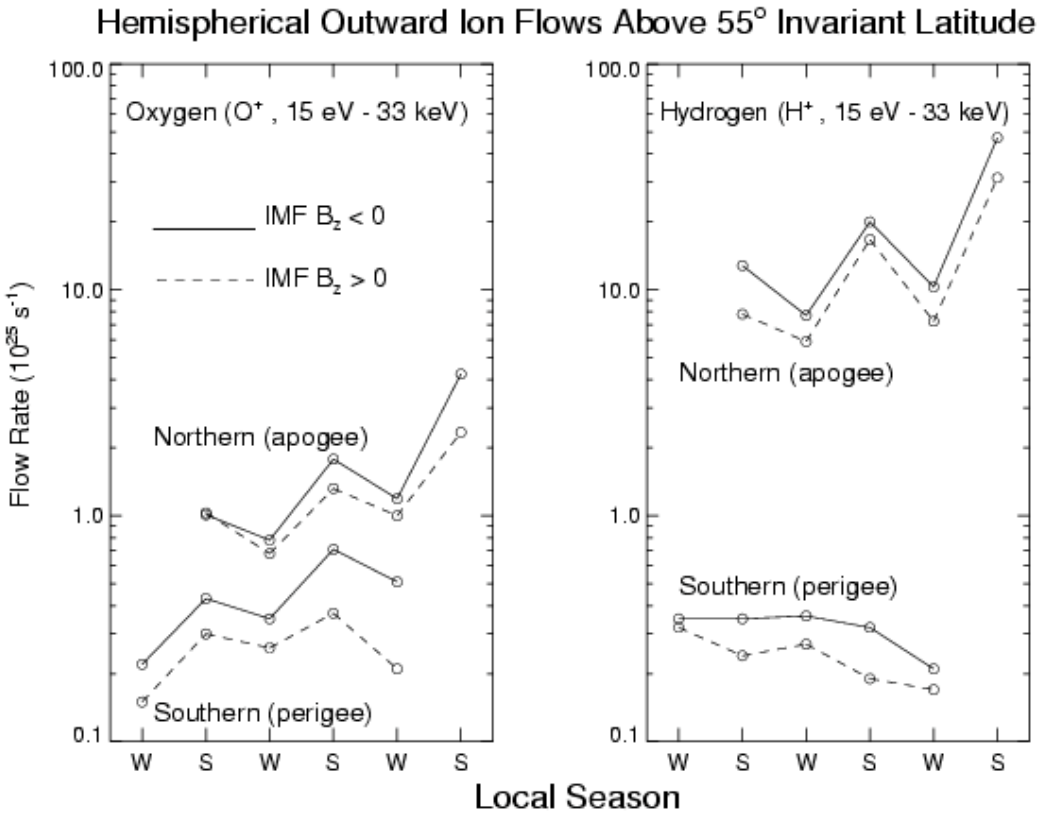

Figure 2. Seasonal (6 months winter W or summer S) average rates of ion outflow in southern (average R(SM) ∪2.2 R_E) and northern (average R(SM) ∪7.5 R_E) hemispheres during 1996-98, subdivided by the preceding 15-minute average IMF B_z polarity (in GSM coordinates). Note: Northern H^+ flow rates are dominated by plasma mantle flow.

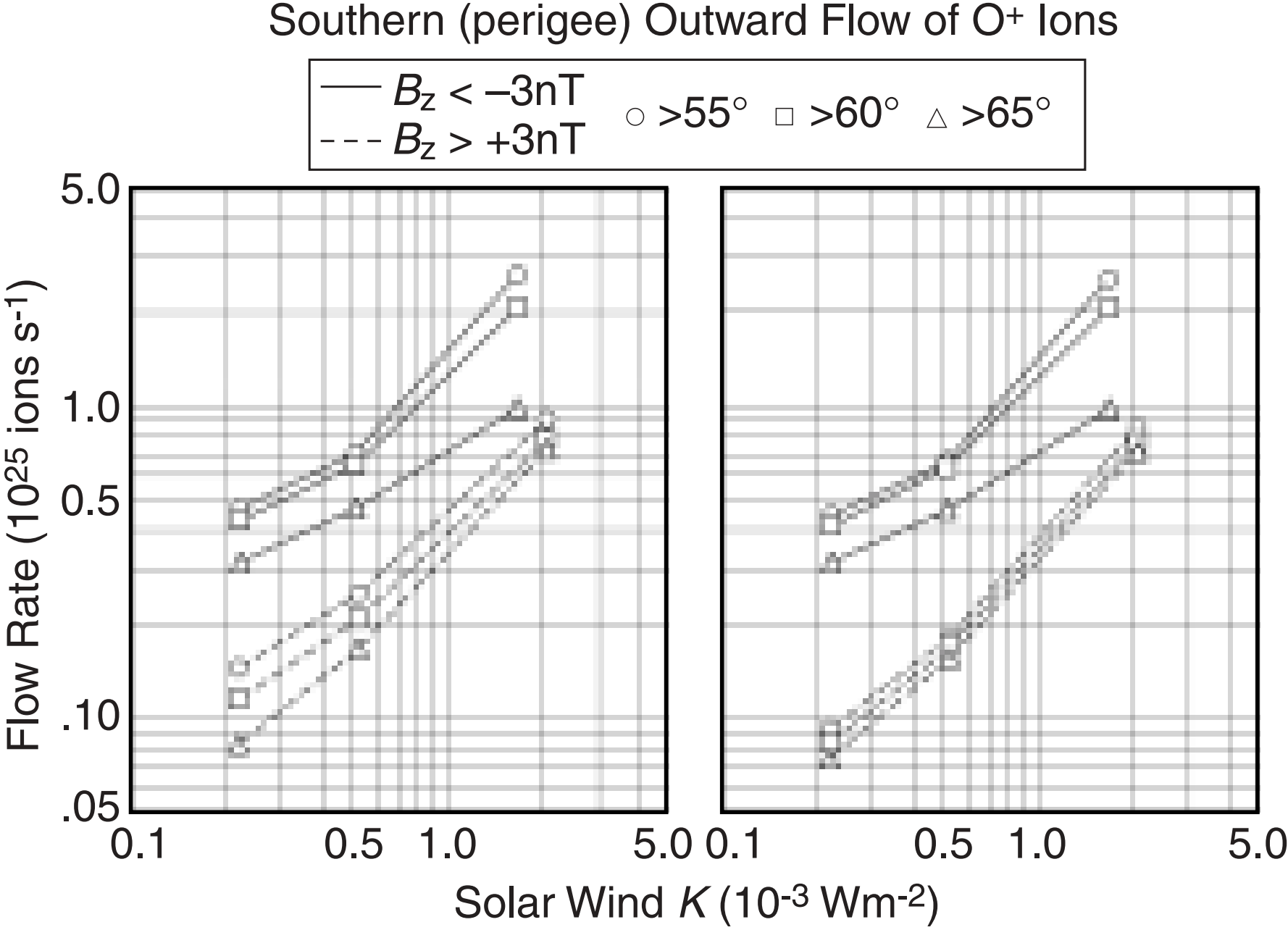

Figure 3. Extended (33 months) average rates of O^+ outflow in the southern hemisphere above each of three different invariant latitudes (55°, 60° and 65°), while (1) the preceding 15-min average solar wind kinetic energy flow density *K* is at certain mean levels (see text), and (2) the associated 15-min average IMF B_z is either positive (dashed lines) or negative (solid lines) by more than 3 nT. Left panel is based on strictly outward flow, treating net earthward flow as zero-flow samplings, right panel includes flows of both signs (see text).

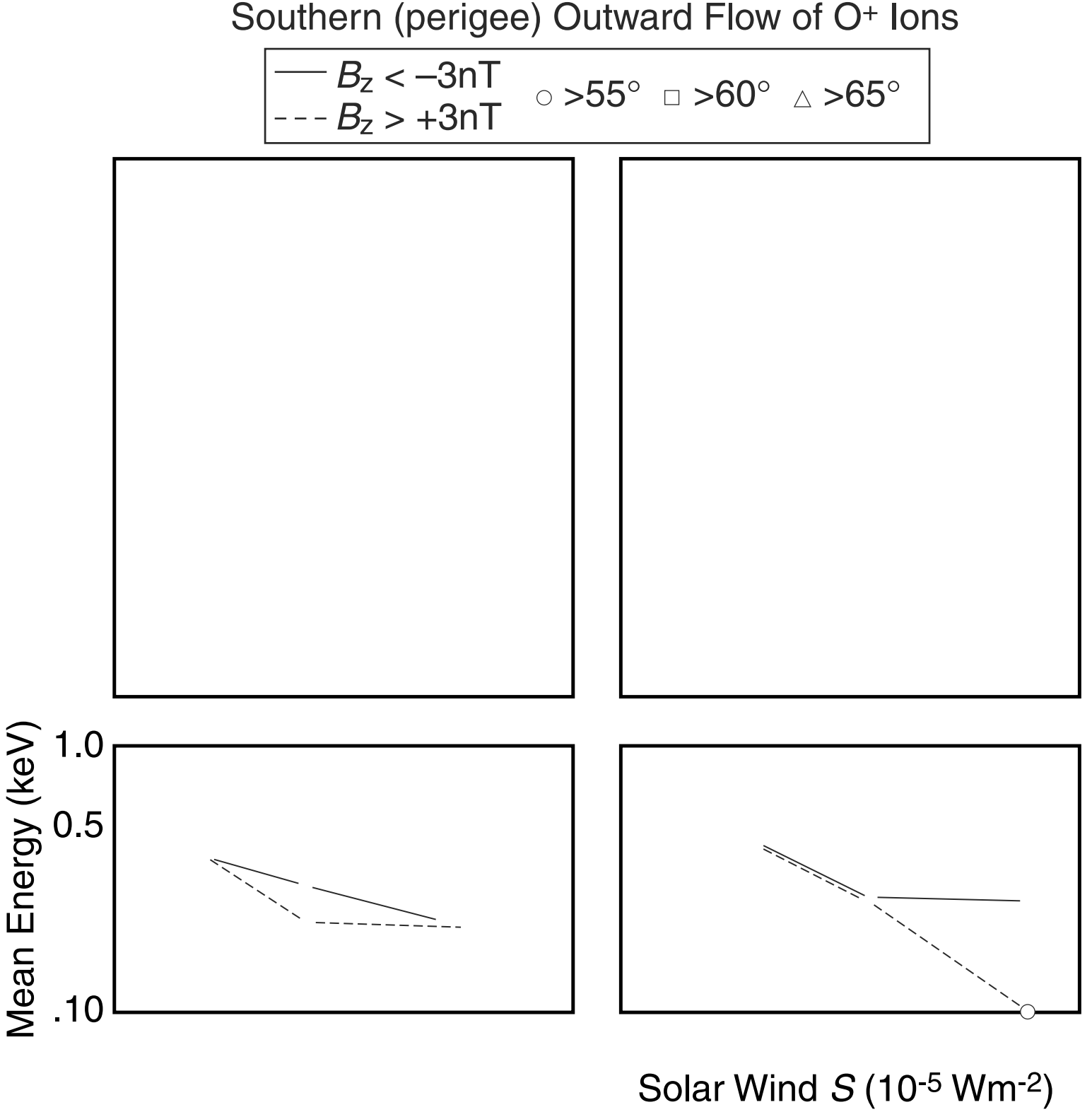

romagnetic (Poynting) energy flow density S (see text). Bottom: Corresponding (> 55°) mean energies, defined as outward energy flow rate divided by number flow rate (error bars reflect spread among the three latitudes, see text).